


 Cite this: *Soft Matter*, 2021, 17, 3619

## Emergent cell-free layer asymmetry and biased haematocrit partition in a biomimetic vascular network of successive bifurcations†

 Qi Zhou,<sup>a</sup> Joana Fidalgo,<sup>b</sup> Miguel O. Bernabeu,<sup>c</sup> Mónica S. N. Oliveira<sup>b</sup> and Timm Krüger<sup>a</sup>

Blood is a vital soft matter, and its normal circulation in the human body relies on the distribution of red blood cells (RBCs) at successive bifurcations. Understanding how RBCs are partitioned at bifurcations is key for the optimisation of microfluidic devices as well as for devising novel strategies for diagnosis and treatment of blood-related diseases. We report the dynamics of RBC suspensions flowing through a biomimetic vascular network incorporating three generations of microchannels and two classical types of bifurcations at the arteriole level. Our microfluidic experiments with dilute and semidilute RBC suspensions demonstrate the emergence of excessive heterogeneity of RBC concentration in downstream generations upon altering the network's outflow rates. Through parallel simulations using the immersed-boundary-lattice-Boltzmann method, we reveal that the heterogeneity is attributed to upstream perturbations in the cell-free layer (CFL) and lack of its recovery between consecutive bifurcations owing to suppressed hydrodynamic lift under reduced flow conditions. In the dilute/semidilute regime, this perturbation dominates over the effect of local fractional flow at the bifurcation and can lead to inherently unfavourable child branches that are deprived of RBCs even for equal flow split. Our work highlights the importance of CFL asymmetry cascading down a vascular network, which leads to biased phase separation that deviates from established empirical predictions.

 Received 15th October 2020,  
 Accepted 1st January 2021

DOI: 10.1039/d0sm01845g

[rsc.li/soft-matter-journal](http://rsc.li/soft-matter-journal)

## 1 Introduction

The human microcirculation is a network of microvessels (involving arterioles, venules and capillaries) perfused by blood to maintain the normal function of organs and tissues.<sup>1</sup> A main feature of the microcirculatory blood flow is its highly heterogeneous haematocrit (or volume fraction of RBCs, *Ht*). This heterogeneity is a direct consequence of disproportionate partitioning of RBCs (relative to the flow split) at successive bifurcations, governed by the well-known Zweifach–Fung effect owing to prevalent CFLs in microvessels.<sup>2,3</sup> Under extreme conditions, some child branches may only receive the plasma from the CFL of the feeding branch and are completely deprived of RBCs, the phenomenon of which is coined by Krogh as *plasma skimming*.<sup>4</sup>

Extensive studies have explored factors that could potentially affect the partitioning of RBCs at vascular/artificial bifurcations, either *in vivo*<sup>5–8</sup> or *in vitro*.<sup>9–15</sup> By using bioplastic bifurcating channels ranging from 20–100  $\mu\text{m}$  in diameter, Fenton *et al.* identified three key variables: the feeding haematocrit, the diameter of vessels, and the fractional flows in respective child branches.<sup>9</sup> The dominance of these variables was further confirmed by Pries *et al.*<sup>8</sup> via examination of multiple arteriolar bifurcations in rat mesentery. Thanks to the abundance of *in vivo* data, Pries *et al.* developed a robust empirical model that provides quantitative description of the phase-separation process at microvascular bifurcations (hereafter referred to as phase-separation model, PSM). Over time, the PSM evolves with refined parametric formulation<sup>16–19</sup> and has been widely applied to elaborate microcirculatory blood flow.

Experimentally speaking, *in vivo* investigation of the phase-separation process is inherently subject to various uncertainties (*e.g.* photometric accuracy, physiological compensation, or regulatory responses). On the other hand, critical challenges also remain to be satisfactorily resolved for *in vitro* experiments (*e.g.* geometric reality, concentration constriction, independent plasma/cell velocimetry and haematocrit determination) to accurately imitate and quantify the process using microfluidic

<sup>a</sup> School of Engineering, Institute for Multiscale Thermofluids, University of Edinburgh, Edinburgh EH9 3FB, UK  
 E-mail: q.zhou@ed.ac.uk, timm.krueger@ed.ac.uk

<sup>b</sup> James Weir Fluids Laboratory, Department of Mechanical and Aerospace Engineering, University of Strathclyde, Glasgow G1 1XJ, UK

<sup>c</sup> Centre for Medical Informatics, Usher Institute, University of Edinburgh, Edinburgh EH16 4UX, UK

† Electronic supplementary information (ESI) available. See DOI: 10.1039/d0sm01845g



bifurcations composed of comparably small channels.<sup>12,13,20,21</sup> These experimental limitations can be potentially overcome by increasingly realistic computational simulations, which can query multiple aspects that are otherwise inconvenient or inaccessible to experiments, such as microscopic cell dynamics in a dense suspension, emergent cell orderings on the cross-sectional plane and spatio-temporal RBC flow properties (e.g. evolving CFLs<sup>22,23</sup>).

However, there is a lack of coordination between experimental and computational studies to converge towards a mutual understanding of the phase-separation process within overlapping parameter space (e.g. channel dimension, fluid inertia, cell concentration, RBC deformability) and under justifiable assumptions (e.g. ideal Poiseuille flow, centralised haematocrit profile, symmetric CFLs). One such discrepancy in understanding haematocrit partition at a bifurcation is about the existence/strength of a potential preference of RBC populations moving towards the orthogonal side branch (rather than the continuation of the parent branch) in the typical right-angle T-bifurcation, for which previous microfluidic<sup>12</sup> and computational<sup>24</sup> studies offered conflicting answers.

For a mechanistic understanding of the phase-separation process, two-dimensional (2D) *in silico* models have been widely employed to study the microscopic behaviour of individual RBCs at a bifurcation.<sup>25–28</sup> Several underlying effects have been proposed, such as the vessel obstruction effect,<sup>29</sup> the unbalanced shear-force effect,<sup>30</sup> the branching angle effect,<sup>31</sup> and the low-flow attraction effect.<sup>32</sup> Recently, three-dimensional (3D) computer simulations considering more realistic cell-wall interactions<sup>24,33–38</sup> emerged to overcome the inherent limitations of 2D models.

Apart from the interaction between RBCs and the bifurcation geometry, the breakdown and recovery of CFLs in pre-/post-bifurcation branches is also an increasing focus of *in silico* studies.<sup>39–41</sup> The RBC core is usually disturbed at a bifurcation, leading to asymmetric CFL associated with transient haematocrit profiles. If the inter-bifurcation distances are short or only moderate (e.g. less than 10 vessel-diameter long as postulated by ref. 8), the transverse organisation of RBCs bears a memory of the transient flow from last bifurcation and the CFL symmetry may not be restored upon reaching the next bifurcation.<sup>23,42,43</sup> Indeed, recent RBC simulations in a microvascular network demonstrated increasingly asymmetric CFL that develop along curved vessels without apparent recovery of symmetry.<sup>22</sup> In line with an earlier *in vitro* study,<sup>12</sup> these simulations also highlighted the profound impact of haematocrit-profile skewness on the partitioning of RBCs at bifurcations in the vascular network.<sup>44</sup> As the symmetry assumption for haematocrit profile in the parent branch of a bifurcation is central to the empirical formulation of PSM,<sup>8</sup> uncertainties arise when applying PSM to bifurcations in a network where time-dependent effects are prevailing, for instance, with underdeveloped cellular flow between successive bifurcations (more likely to occur with smaller inter-bifurcation distances and lower RBC concentrations).

The present study aims to elucidate the phase separation of blood flow in bifurcating networks by inspecting the partitioning

of dilute/semidilute RBC suspensions through successive bifurcations under controlled outflow conditions, where cell-cell interactions are weak and the microscopic behaviour of individual RBCs can be tracked experimentally. We perform experiments and simulations of a biomimetically designed artificial vascular network that comprises three generations of microchannels with two classical types of bifurcations. Through cross-validation of experimental and simulation data, we uncover an emerging heterogeneity of haematocrit partition within the network that substantially deviates from empirical predictions of the PSM. We attribute this heterogeneity to the perturbed CFLs between bifurcations and analyse the underlying RBC dynamics subject to network outflows. It is found in the dilute/semidilute regime, upstream CFL perturbations persist and can lead to severely biased phase-separation at a bifurcation under reduced flow conditions, even with equal fractional flow for the child branches. Furthermore, we identify consistent patterns of haematocrit reduction/enrichment in the network against varying outflow ratios for different systemic haematocrits, which may provide insights into the elusive microvascular blood flow, and inspire the optimisation of existing microfluidic devices for handling RBC suspensions.

## 2 Materials and methods

### 2.1 Microfluidic experiments

Fig. 1a shows a typical microfluidic network used in this work. The planar microdevice was manufactured in PDMS (polydimethylsiloxane, Sylgard 184, Dow Corning) by soft-lithography using an SU8 mould produced by photo-lithography (microLIQUID), and was sealed with a glass slide substrate using oxygen plasma treatment (Zepto, Diener). Each network is composed of three generations. The 0th generation ( $i = 0$ ) has one main channel, which is hereafter referred to as the network parent branch (PB). The PB bifurcates into two child branches (CBs) in the 1st generation ( $i = 1$ ), which are denoted CB11 and CB12, respectively. CB11 and CB12 themselves further bifurcate in the 2nd generation ( $i = 2$ ), leading to four child branches denoted CB21, CB22, CB23 and CB24, respectively. All channels have a constant depth  $H = 30 \mu\text{m}$ . The channel width  $W_i = 96, 50.5, 30 \mu\text{m}$  varies following the biomimetic rule proposed by<sup>45,46</sup> so that a generalised Murray's law for microfluidic manifolds is observed, which yields a constant wall shear stress in the fully developed regions throughout the network (see Fig. S1 in the ESI† for numerical validation). The segment length  $L_i$  is designed as  $L_i = 10D_{h,i}$ , where  $D_{h,i} = 2W_iH/(W_i + H)$  is the hydraulic diameter of a given branch (except  $i = 0$ , where  $L_0 = 30D_{h,0}$ ). The main difference between the current design and the ones proposed in ref. 45 and 46 is the bifurcation angle, which is chosen as 90 degrees, rather than 180 degrees, to avoid sharp bends within child branches.<sup>47,48</sup> A second device with an angle of 60 degrees at all bifurcations has also been fabricated to test the effect of bifurcation angle (see Fig. S2a in the ESI†).

The blood samples consist of RBC suspensions in Dextran40, prepared using horse blood in anticoagulant EDTA



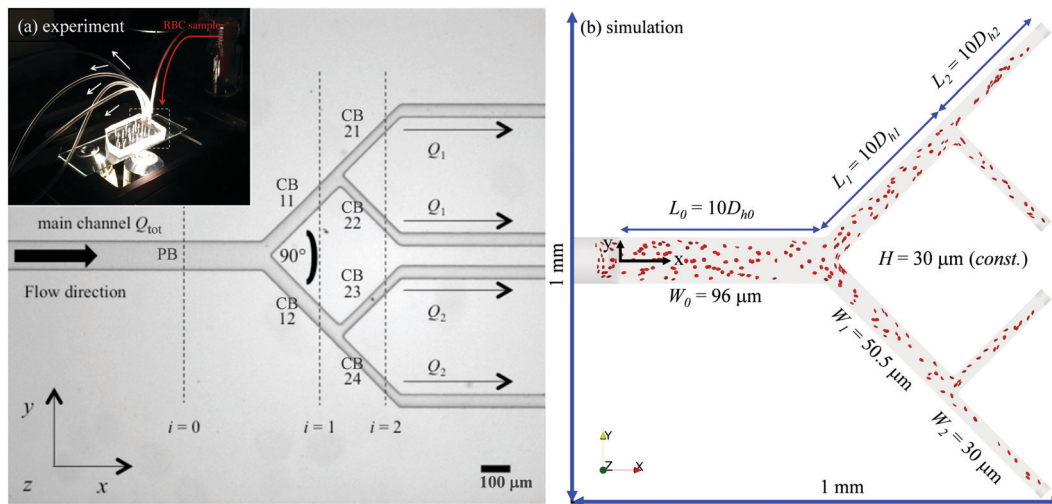


**Fig. 1** (a) Photomicrograph of the microfluidic device (main frame) and digital image of the experimental setup (inset), showing the connection of the microfluidic device to RBC samples and syringe pumps. Two volume flow rates  $Q_1$  and  $Q_2$  are imposed at the outlets, and the resulting total volume flow rate in the system is  $Q_{\text{tot}}$  (measured at the parent branch PB); all bifurcation angles for this design are 90 degrees. Scale bar is 100  $\mu\text{m}$ . (b) A snapshot of the simulation with flow ratio  $Q_2/Q_1 = 1$ , showing the computational domain and RBCs continuously fed with a fixed volume fraction of 1% at the inlet.

(TCS Biosciences,  $1.5 \text{ mg mL}^{-1}$ ). The sample-processing procedures have been detailed in our previous work<sup>49</sup> and are therefore not repeated here for brevity. The steady shear rheology of Dextran 40 was determined by a rotational rheometer (DHR2, TA Instruments, with minimum resolvable torque 0.1 nN m) using a cone-plate geometry of 60 mm diameter and angle  $\theta = 1^\circ$  (CP60/1), 30  $\mu\text{m}$  truncation gap. The density and shear viscosity are  $1.07 \times 10^3 \text{ kg m}^{-3}$  and 5.0 mPa s, respectively.

The flow of the RBC suspensions through the device was imposed using two syringe pump modules (Nemesys, Cetoni) connected to the outlets. These modules can be operated independently (one for  $Q_1$ , the other for  $Q_2$  as depicted in Fig. 1a) and each module controls two coupled syringes continuously withdrawing the RBC sample from the single inlet. Flow visualisation was performed using an inverted microscope (Olympus IX71) equipped with a halogen lamp. Videos/images were acquired by a sensitive monochrome CCD camera (Olympus, XM10) using a  $10\times$  magnification objective with numerical aperture of 0.25 to guarantee that the depth of field and image depth are large enough to observe cell trajectories across the entire channel height.

## 2.2 Numerical simulation

The computational domain for numerical simulations is reconstructed using design dimensions of the microfluidic device (see Fig. 1b and Table 1). The flow inlets/outlets are modelled as cylindrical regions with the same geometry as the CTRACT-S configuration (“smaller inflow contraction”) of the microchannel simulated in our previous work.<sup>49</sup> This geometric feature enables an RBC distribution with considerate initial CFLs upon entry into the main channel, therefore a much shorter length of the parent branch PB ( $\approx 10D_{h,0}$ ) than its experimental counterpart ( $= 30D_{h,0}$ ) is needed for the CFL to fully develop before reaching the first bifurcation. This treatment is crucial, as an equivalent length of the numerical PB to the experimental one

would be prohibitively expensive for cellular simulation. To initialise the simulation, a plasma flow (without RBCs) is pulled from left to right with a fixed volume flow rate  $Q_{\text{tot}} = 4 \mu\text{L min}^{-1}$  in PB with varying outflow ratio  $Q_1/Q_2$ . This is realised by imposing parabolic velocity profiles (assuming Poiseuille flow in the cylindrical extensions, with no-slip condition on the channel wall) at each outlet. After the steady flow has been established within the whole network, RBCs are randomly inserted from the cylindrical entry region in a continuous manner with fixed feeding haematocrit of 1%, 2% or 10%.

**Table 1** (Simulation) Key parameters for simulation setup. The symbols “~” represent dimensionless simulation units

| Network geometry                     |   |                                 |
|--------------------------------------|---|---------------------------------|
| Channel width                        | $W_i (i = 0, 1, 2)$   | 96, 50.5, 30 $\mu\text{m}$      |
| Channel depth                        | $H$   | 30 $\mu\text{m}$                |
| Network length                       | $L$   | 1 mm                            |
| Hydraulic diameter                   | $D_{h,i}$   | $2W_iH/(W_i + H)$               |
| RBC model                            |   |                                 |
| Cell radius                          | $r_{\text{rbc}}$  | 4 $\mu\text{m}$                 |
| Viscosity contrast                   | $\lambda$   | 1.0                             |
| Feeding haematocrit                  | $H_F$   | 1%, 2%, 10%                     |
| Local haematocrit                    | $\phi$  | variable                        |
| Simulation setup                     |   |                                 |
| Particle Reynolds number ( $i = 0$ ) | $\text{Re}_p$   | 0.03                            |
| Capillary number ( $i = 0$ )         | Ca  | 0.6                             |
| LB relaxation parameter              | $\tilde{\tau}_{\text{BGK}}$   | 1.0                             |
| Voxel size                           | $\Delta x$  | 0.6667 $\mu\text{m}$            |
| Time step                            | $\Delta t$  | $7.41 \times 10^{-8} \text{ s}$ |
| Shear modulus                        | $\tilde{\kappa}_s$  | $5.00 \times 10^{-4}$           |
| Bending modulus                      | $\tilde{\kappa}_b$  | $4.50 \times 10^{-5}$           |
| Reduced bending modulus              | $\tilde{\kappa}_b \Delta x^2 / (\tilde{\kappa}_s r_{\text{rbc}}^2)$ | 1/400                           |
| Cell-cell interaction                | $\tilde{\kappa}_{\text{cc}}$  | $\tilde{\kappa}_b$              |
| Cell-wall interaction                | $\tilde{\kappa}_{\text{cw}}$  | $10\tilde{\kappa}_b$            |



The numerical model for simulating blood flow as a suspension of deformable RBCs as in our recent work<sup>49</sup> employs the immersed-boundary-lattice-Boltzmann method (IB-LBM<sup>50</sup>). The model is implemented in the parallel flow simulator *HemeLB*<sup>51,52</sup> (open source at <https://github.com/hemelb-codes/hemelb>) by incorporating a new module for discrete deformable cells. The fluid flow governed by the Navier–Stokes equations is solved by the lattice-Boltzmann method with standard D3Q19 lattice,<sup>53</sup> BGK collision operator,<sup>54</sup> Guo's forcing scheme<sup>55</sup> and the Bouzidi–Firdaouss–Lallemand (BFL) implementation of no-slip boundary condition at the walls.<sup>56</sup> To precisely control the volume flow rates at various inlets/outlets, inflow/outflow open boundary conditions are implemented with the Ladd velocity boundary condition.<sup>57</sup>

The RBCs are modelled as Lagrangian membranes through a finite element approach, which are further coupled with the fluid flow using the immersed-boundary method<sup>58</sup> for the interpolation of velocities and the spreading of forces. Each RBC is modelled as a closed finite-element membrane consisting of 720 triangular facets (with the membrane mesh matching the lattice resolution  $\Delta x$  for numerical stability and accuracy<sup>59</sup>). The unstressed RBC shape is assumed as a biconcave discoid. The RBC membrane is elastic, with its mechanical properties controlled by five moduli which govern different energy contributions. They are the strain modulus  $\kappa_s$ , the bending modulus  $\kappa_b$ , the dilation modulus  $\kappa_\alpha$ , the surface modulus  $\kappa_S$  and the volume modulus  $\kappa_V$ . To tackle potential close-contact of cells or between a cell and the wall, a repulsion potential decaying with inverse distance between neighbouring surfaces is implemented (characterised by interaction strengths  $\kappa_{cc}$  and  $\kappa_{cw}$  as in Table 1).

The flow behaviour of RBCs is determined by the particle Reynolds number  $Re_p$  and the capillary number  $Ca$ .  $Re_p$  represents the ratio of particle inertia to fluid viscous forces and is defined based on the channel Reynolds number  $Re_c$ :

$$Re_p = Re_c(2r_{\text{rbc}}/D_h)^2, \quad Re_c = \rho_{\text{ex}}\bar{u}D_h/\eta_{\text{ex}} \quad (1)$$

where  $r_{\text{rbc}}$  is the RBC radius and  $D_h$  is the hydraulic diameter of the rectangular channel;  $\bar{u}$  is the cross-sectional mean velocity of the unperturbed flow;  $\rho_{\text{ex}}$  and  $\eta_{\text{ex}}$  are the density and dynamic viscosity of the suspending fluid, respectively.  $Ca$  represents shear-induced deformation of the RBC membrane and is defined using its shear modulus  $\kappa_s$ :

$$Ca = \tau_{\text{rbc}}\dot{\gamma}_c, \quad \tau_{\text{rbc}} = \eta_{\text{ex}}r_{\text{rbc}}/\kappa_s, \quad \dot{\gamma}_c = 8\bar{u}/D_h \quad (2)$$

where  $\tau_{\text{rbc}}$  is a characteristic time scale for the RBC membrane to relax to its equilibrium shape from a transient state and  $\dot{\gamma}_c$  is the characteristic wall shear rate in equivalent Poiseuille flow. Both  $Ca$  and the viscosity contrast  $\lambda$  (between RBC cytosol and the suspending fluid) are kept the same for experiments and simulations (see Table 1).

### 2.3 Cell-counting procedure

The quantification of RBC fluxes  $Q_{\text{rbc}}$  in the network relies on a cell-counting procedure that records cells crossing designated planes of interest, which are placed perpendicular to the channel axis of individual branches. To satisfy mass conservation, the counting procedure only considers RBCs outwith the

transient state of a simulation, *i.e.* when the total number of cells in the simulated network has become quasi-constant. The obtained  $Q_{\text{rbc}}$  values are then used to calculate the discharge haematocrit  $H_D$  in each branch based on the local volume flow rate of blood  $Q_{\text{blood}}$ . To describe the systematic variation of RBC concentration within the vascular network, we follow the approach of Pries *et al.*<sup>60</sup> and compare the  $H_D$  value of a given child branch against that of PB (referred to as  $H_{D,\text{inflow}}$ ). Note that  $H_{D,\text{inflow}}$  should not be confused with  $H_F$ , which is the feeding haematocrit from our numerical inlet imitating a RBC reservoir and may differ slightly from  $H_{D,\text{inflow}}$ . If  $H_D/H_{D,\text{inflow}} < 1$  for the child branch, this is defined as haematocrit reduction; if  $H_D/H_{D,\text{inflow}} > 1$ , this is defined as haematocrit enrichment. For the calculation of local haematocrits  $\phi$ , which are needed to construct cross-sectional haematocrit profiles, cells are extracted at given time intervals (sufficiently large to minimise the effect of cell sampling) from the simulation after steady state has been reached.

## 3 Results

### 3.1 Outflow-tuned RBC distribution and CFL asymmetry

**3.1.1 Experiments.** The partitioning of RBCs within the network is investigated using three different values for the feeding haematocrit ( $H_F$ ):  $H_F = 1\%$ ,  $10\%$ ,  $20\%$  (Fig. 2a and Fig. S3, ESI†). In the standard experimental setting of  $Q_2/Q_1 = 1$ , lateral CFLs can be clearly observed next to the side walls of the PB under  $H_F = 1\%$ . The CFLs become less prominent under  $H_F = 10\%$  and negligible under  $H_F = 20\%$  (Fig. 2b).

In experiments with  $H_F = 1\%$ , where  $Q_1 = 0.2 \mu\text{L min}^{-1}$  is kept constant while gradually increasing  $Q_2$  to achieve higher flow ratios ( $Q_2/Q_1 = 1\text{--}40$ , see the variation of flow pathlines in Fig. S4a–c, ESI†), diverse patterns of RBC distribution are achieved at successive bifurcations (Fig. 2c). Fig. 3a details the RBC distribution at  $Q_2/Q_1 = 40$  (as in the last panel of Fig. 2c). Notably, despite an even flow split for CB21 and CB22, a marked discrepancy in RBC concentration exists between them, potentially caused by the one-sided RBC core in CB11. Inspection of the intensity profiles reveals that the CFLs measured at a fixed location in the PB remain constant and symmetric, regardless of the varying outflow ratio (see the overlapping intensity peaks in Fig. 3b for  $Q_2/Q_1 = 1\text{--}40$ ). On the contrary, in CB11 (Fig. 3c) and CB21 (Fig. 3d), a sharp CFL asymmetry develops, with pronounced CFLs present near one side of the channel wall and virtually no CFLs near the other. At  $Q_2/Q_1 = 20$ , the outward CFL in CB21 occupies nearly half of the channel width (see blue curve in Fig. 3d). Further increasing the flow ratio to  $Q_2/Q_1 = 40$  leads to the expansion of the CFL across the whole channel width (see purple curve in Fig. 3d), corresponding to the complete depletion of cells observed in Fig. 3a. Subsequent quantification shows that the trend of CFL expansion in CB21 *versus* the network outflow ratio is almost linear (Fig. 3e).

An identical trend is observed if  $Q_1 = 2.0 \mu\text{L min}^{-1}$  is fixed instead while increasing  $Q_2$ , or having  $Q_{\text{tot}} = 0.8 \mu\text{L min}^{-1}$  fixed while changing both  $Q_1$  and  $Q_2$  to achieve the desired  $Q_2/Q_1$  (Fig. 3e). Experiments conducted in the microfluidic device



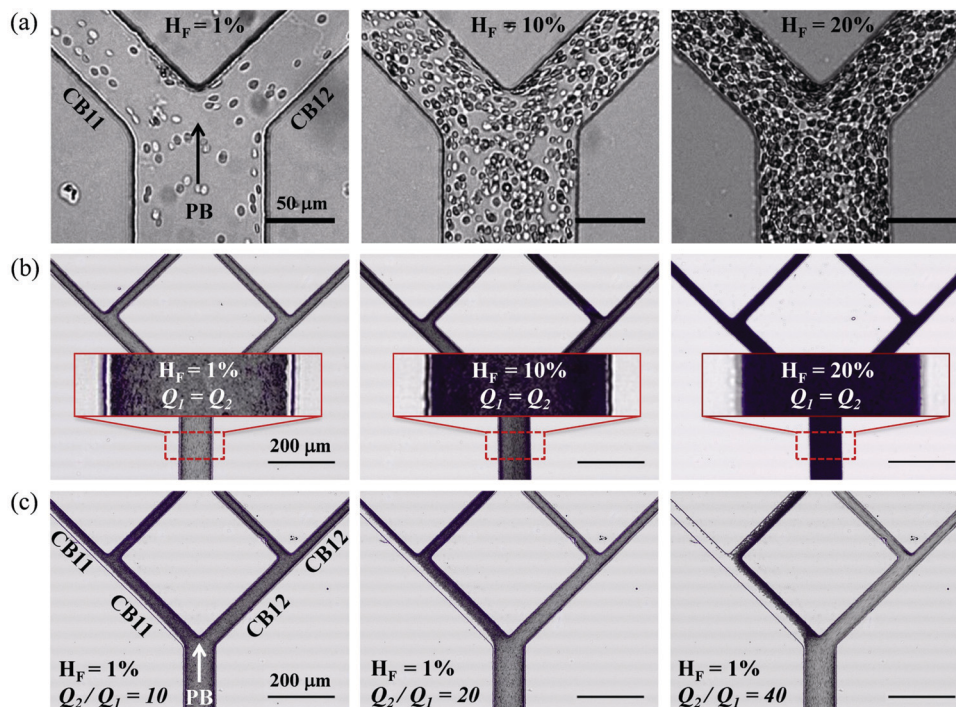


**Fig. 2** (Experiment) (a and b) Comparison between RBC suspensions of different nominal feeding hematocrits ( $H_F = 1\%$ ,  $10\%$ ,  $20\%$ ) flowing through the network for  $Q_1 = Q_2 = 0.2 \mu\text{L min}^{-1}$ . The flow rates are controlled through the four outlets. (a) Individual frames showing the RBCs in the region of the first bifurcation at different  $H_F$ . Scale bar  $50 \mu\text{m}$ . (b) Composite images obtained using the Z-projection method (minimum intensity), each combining 500 frames of the same region. The inset shows the enlarged view of a region in the parent branch (marked by a dashed rectangular box) for visual detection of CFLs. Scale bar  $200 \mu\text{m}$ . (c) RBC distribution under different outflow ratios  $Q_2/Q_1 = 10, 20, 40$  (with  $Q_1 = 0.2 \mu\text{L min}^{-1}$  fixed) at  $H_F = 1\%$ . The scale bar is the same as in (b). Note that all experimental images in this figure have been rotated by  $90$  degrees for visual clarity.

with  $60$ -degree bifurcations also present the same trend (Fig. 3f and Fig. S2b, c, ESI<sup>†</sup>). These findings suggest that neither the flow rate in the parent branch nor the bifurcation angles play an important role in the RBC partitioning within the designed

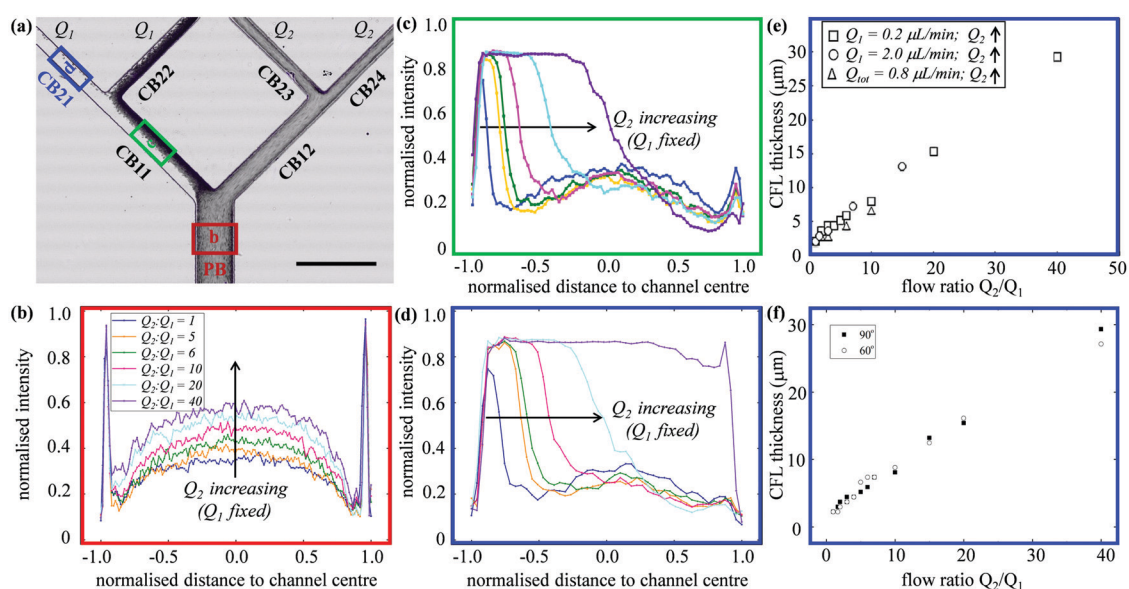


**Fig. 3** (Experiment) (a) Composed experimental image (rotated by  $90$  degrees) combining  $300$  video frames using the Z-projection method (minimum intensity).  $Q_1 = 0.2 \mu\text{L min}^{-1}$  and  $Q_2 = 8.0 \mu\text{L min}^{-1}$ . Scale bar  $200 \mu\text{m}$ . (b-d) Intensity profiles (as an indicator of RBC distribution) obtained from three regions of interest (ROIs) as a function of the flow rate ratio  $Q_2/Q_1$  (with  $Q_1 = 0.2 \mu\text{L min}^{-1}$  fixed). These ROIs are located in (b) PB as marked by the red box in (a); (c) CB11 as marked by the green box in (a); (d) CB21 as marked by the blue box in (a). Intensity peaks in (b-d) indicate zones free of cells. (e and f) CFL measured in channel CB21 as a function of the flow rate ratio  $Q_2/Q_1$  for the network geometries of bifurcation angle  $90$  degrees and  $60$  degrees, respectively. All data in this figure are for  $H_F = 1\%$ .



bifurcating network, at least for  $Q_1$  between 0.2 and 2.0  $\mu\text{L min}^{-1}$ , and the bifurcation angle between 60 and 90 degrees.

**3.1.2 Simulations.** To understand the RBC partitioning behaviour observed in experiments and provide mechanistic insights, an equivalent system of RBC flow is simulated with fixed volume flow rate  $Q_{\text{tot}} = 4.0 \mu\text{L min}^{-1}$  in the PB and with varying flow ratio  $Q_2/Q_1$  at the outlets (see Table S1 in the ESI†). The present cellular simulations with fully bounded pressure-driven channels (by solid walls in both depthwise and spanwise directions) reproduce the RBC polylobes (see Fig. S5g and h in the ESI†) experimentally observed in microfluidic channels of different cross-sections,<sup>61–63</sup> which have only been verified by numerical simulations with simple shear flow or planar Poiseuille flow previously.

As  $Q_2/Q_1$  increases, we find similar variation of the RBC fluxes (represented by cell trajectories) within the bifurcating network to experiments (Fig. 4a–d). The RBC fluxes in the upper-half child branches of the network (CB11, CB21 and CB22), where the flow rates are considerably smaller than their counterparts in the lower-half child branches (CB12, CB23 and CB24), gradually diminish as  $Q_2/Q_1$  increases. At  $Q_2/Q_1 = 19$ , the terminal branch CB21 is completely devoid of cells (Fig. 4c). Further increasing the flow ratio to  $Q_2/Q_1 = 39$  leaves both branches CB21 and CB22 free of cells (Fig. 4d).

Next, we quantify the distribution of RBC fluxes at the primary Y-bifurcation (referred to as BifY hereafter). The fractional RBC fluxes  $Q_{\text{rbc}}^*$  in the child branches CB11 and CB12 (relative to the

RBC flux in PB) are calculated and evaluated against the empirical PSM<sup>17</sup> as described in eqn (S1)–(S4) (see Section S6 of the ESI†). Good agreement is found between the simulation data and the empirical predictions, with the relative errors under all tested flow conditions below 1% (see Table S2 in the ESI†). The quantitative match suggests that our simulated RBC partitioning at BifY sensibly reproduces the Zweifach–Fung effect. Furthermore, it can be inferred that for the present channel dimensions at BifY ( $D_h = 30\text{--}50 \mu\text{m}$ ), where the cells are not strongly confined, the effect of fractional flow on RBC distribution dominates over that of channel geometry (rectangular instead of circular here).

One intriguing feature found in the RBC trajectories at the geometrically symmetric BifY is a protrusion cap into the lower-flow branch (marked with dotted circles in panels “1”–“4” of Fig. 4). Such protrusion of cell trajectories indicates a diversion of RBC fluxes occurring near the bifurcation apex (or bifurcating point), with cells intending to enter the lower-flow branch abruptly pulled away and diverted towards the higher-flow branch instead. The size of this trajectory protrusion is seemingly correlated with the flow split at BifY (to be elaborated in Section 3.2) and increases with  $Q_2/Q_1$  until complete absence of RBCs in CB11 at  $Q_2/Q_1 = 39$ , causing the deprivation of cells in the entire upper half of the network (CB11, CB21 and CB22).

In line with the experimental findings, two lateral CFLs symmetric about the channel axis exist in the PB at  $H_F = 1\%$  (see Fig. S6 and S7 in the ESI†). CFLs are also found near the

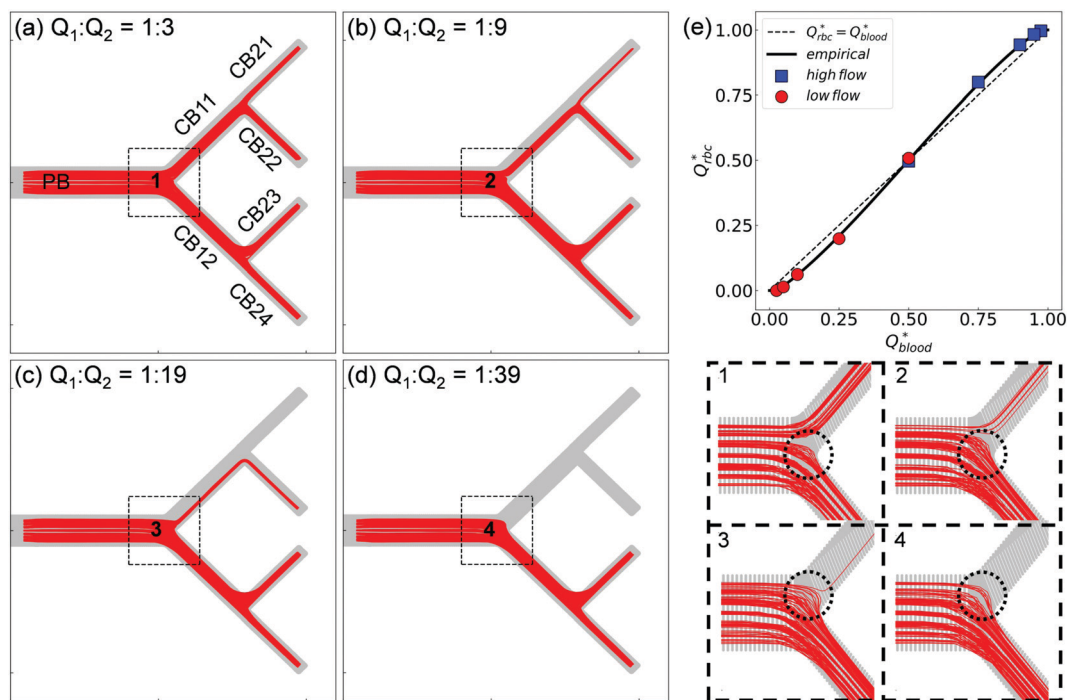


**Fig. 4** (Simulation) RBC fluxes in the network under different flow conditions at  $H_F = 1\%$ . (a–d) Show the superimposed RBC trajectories for flow ratios  $Q_2/Q_1 = 3, 9, 19$ , and 39, respectively. The panels labelled “1”–“4” show enlarged views of the Y-bifurcation region (marked with black dashed square boxes) with a reduced number of trajectories (about 150 randomly selected cell paths) for better clarity. (e) Comparison of the simulated distribution of RBC fluxes against the empirical model.<sup>17</sup>  $Q_{\text{rbc}}^*$  and  $Q_{\text{blood}}^*$  are the fractional RBC flux and fractional blood flow in a child branch relative to its parent branch. The circles and squares represent the relatively lower-/higher-flow child branches within a given bifurcation, respectively. The solid line is the empirical prediction, and the dotted line indicates a linear correlation.



top/bottom walls in the depth direction, which is inaccessible to experimental observation with the present set-up. The CFLs in PB appear independent of the outflow ratio  $Q_2/Q_1$ , either in terms of absolute magnitude and spatial development (which is expected given the fixed flow in PB). Conversely, CFLs in branches of the first generation (namely CB11 and CB12) show a clear dependence on  $Q_2/Q_1$  (Fig. 5). Also, the CFL symmetry between opposite walls appears broken after BifY.

For quantification of the CFL asymmetry, we have defined “inner wall” as the side of a child branch directly connected to the bifurcation apex, and “outer wall” as the opposite side of the same channel. The outer wall of a child branch naturally inherits the CFL from its upstream parent and therefore has initially large CFL thickness. Contrarily, the inner wall usually experiences the

re-establishment of a CFL from zero, which results from direct collision of the core of RBCs in the parent branch with the apex of the bifurcation. The difference between the inner-/outer-wall CFLs (defined as CFL asymmetry) of CB11 is found prominent at high flow ratios, *e.g.*  $Q_2/Q_1 = 9$  or  $Q_2/Q_1 = 19$  (Fig. 5a and b). Furthermore, this asymmetry decreases slowly along CB11 (Fig. 5c) and practically persists throughout the whole branch. On the contrary, CB12 (which receives higher fraction of blood flow than its counterpart CB11) experiences substantially smaller CFL asymmetry (Fig. 5d and e) and faster recovery of CFL symmetry (Fig. 5f).

### 3.2 Diversion of RBC flux at primary Y-bifurcation

To elucidate the occurrence of RBC flux diversion at the primary BifY and the post-bifurcation CFL asymmetry as revealed in

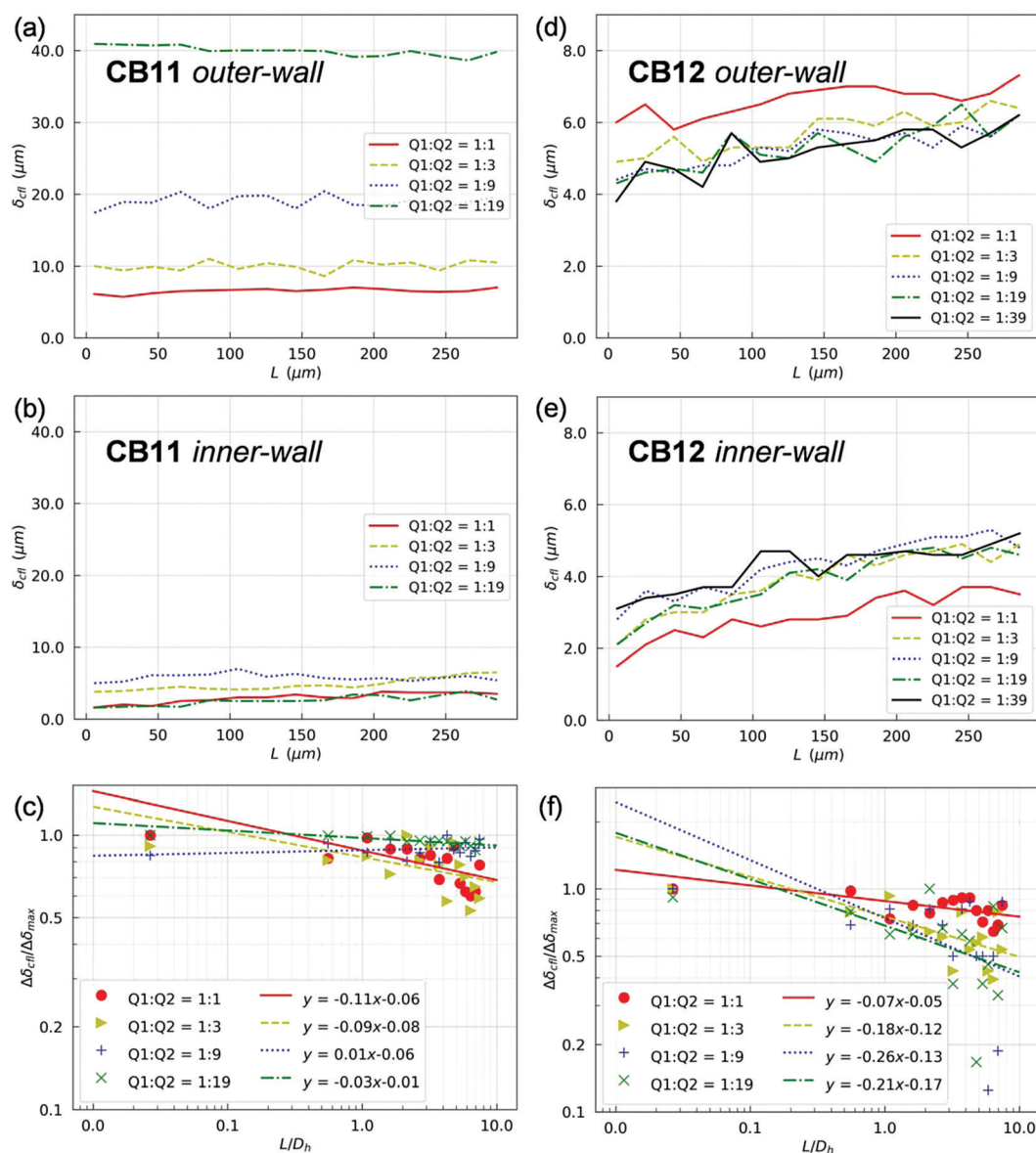


Fig. 5 (Simulation) CFLs along the inner-/outer-walls of (a and b) CB11 and (d and e) CB12 in the first generation of the bifurcating network at  $H_f = 1\%$ . The plots are presented as the CFL thickness  $\delta_{cfl}$  against the development length  $L$  (which represents the axial distance from the upstream bifurcation in the context here). (c and f) present regression analysis of the CFL asymmetry throughout CB11 and CB12, respectively.



Section 3.1.2, we investigate the flow patterns underpinning the RBC motion. From the unperturbed flow field (Fig. 6a–c), the breakdown of flow symmetry and emergence of disrupted streamlines near the bifurcation apex (branching point A in Fig. 6a) is evident as  $Q_2/Q_1$  gradually increases from 1. One notable feature is the appearance of a different separation point A' on the channel mid-plane (located at  $L_s$  away from the branching point A), where the stagnation streamline meets the wall. All streamlines to the right of the stagnation streamline ("right" and "left" determined by a forward view along the flow direction) enter the high-flow branch (*i.e.* bottom branch in the figure), whereas those to its left end in the low-flow branch (*i.e.* top branch in the figure). As  $Q_2/Q_1$  increases, A' shifts towards the low-flow branch, thus increasing the separation distance  $L_s$ , and an enlarged nose tip of curved streamlines in the bifurcation region emerges, which matches the protrusion cap observed in the RBC trajectories (see panels "1"–"4" of Fig. 4).

The RBCs approaching the bifurcation essentially follow the streamlines, and no evident cross-streamline migration of RBC populations is observed from the simulation (see Fig. S4d–f in the ESI†). This explains why the partitioning of RBCs at the Y-bifurcation (where the CFL is symmetric and confinement is small) obeys the classic Zweifach–Fung effect. Consequently, the PSM,<sup>8,16</sup> as an empirical representation of the Zweifach–Fung effect derived from *in vivo* data, can correctly predict the distribution of RBC fluxes at the BifY (see Fig. 4e).

Under high flow ratios  $Q_2/Q_1$ , only a small proportion of streamlines originally close to the PB wall are directed into the low-flow branch CB11, which causes excessive bending of streamlines to satisfy flow continuity (see Fig. S4f in the ESI† for  $Q_2/Q_1 = 39$ ). The streamlines ending in the low-flow branch CB11 largely originate from the outer-wall CFL in PB and therefore carry only a few RBCs. As demonstrated in Fig. 6d–f, due to the severely bent streamlines at  $Q_2/Q_1 = 19$ , the single RBC entering CB11 traverses across the whole channel width of CB11 and moves along its inner wall thereafter. Meanwhile, the protrusion zone is so profound that the other two RBCs already travelling deep into CB11 revert their paths, linger against the bifurcation and eventually proceed towards the higher-flow branch CB12. As the flow ratio increases to  $Q_2/Q_1 = 39$  and the flow rate in the lower-flow branch further drops, all streamlines entering CB11 are from the upstream CFL and carry no RBCs at all (see Fig. S4f in the ESI†).

### 3.3 Biased phase separation at secondary T-bifurcations

Contrary to what happens at the primary BifY, the partitioning of RBC fluxes at the two secondary T-type bifurcations (referred to as BifT1 and BifT2 hereafter) considerably deviates from the empirical predictions based on the Zweifach–Fung effect (see Fig. 7a for BifT1 and Fig. S8 in the ESI† for BifT2). The deviation is particularly severe at BifT1 (Fig. 7a), for which one of the two downstream child branches can be completely depleted of RBCs whereas RBC perfusion is still visible in the other branch

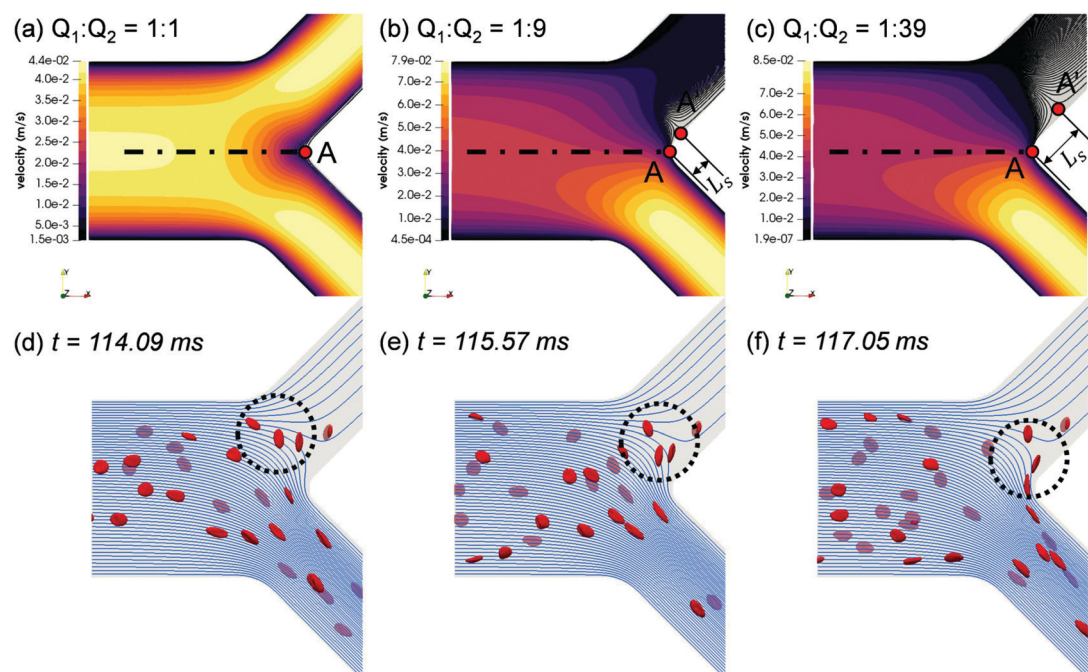


**Fig. 6** (Simulation) (a–c) Velocity contour (horizontal mid-plane) in the Y-bifurcation region at flow ratios  $Q_2/Q_1 = 1, 9$ , and  $39$ , respectively. Colour indicates velocity magnitude. The top branch in all figure panels represents the child branch with a lower flow rate. Steady and unperturbed streamlines (without RBCs) are shown for the lower-flow branch at  $Q_2/Q_1 = 9, 39$ . Point A indicates the bifurcation apex (or branching point); point A' indicates the position where the stagnation streamline (intersection of the separatrix and the channel mid-plane) meets the wall;  $L_s$  is the axial distance between A and A'. (d–f) Time sequence of three tracked RBCs under  $Q_2/Q_1 = 19$  at  $t = 114.09$  ms,  $115.57$  ms, and  $117.05$  ms, respectively.  $H_f = 1\%$ . The background shows the unperturbed streamlines on the channel mid-plane. RBCs beneath the mid-plane are faded.





(compare CB21 and CB22 in Fig. 4c, where  $Q_2/Q_1 = 19$ ). This severely biased partitioning of RBCs would appear counter-intuitive if we simply focused on the local flow split at the bifurcation, which is even for CB21 and CB22.

Underlying this deviation from the empirical approximation at BifT1 is the substantially asymmetric CFL in its feeding branch CB11 (see Fig. 5a–c) as a consequence of the upstream disruption to the cross-sectional RBC distribution by BifY. Recalling our analysis in Section 3.2, this asymmetry primarily arises from the manner how RBCs enter CB11 at BifY, which is sensitive to the outflow ratio  $Q_2/Q_1$  of the network. At sufficiently high  $Q_2/Q_1$ , the RBCs entering branch CB11 (if any) are found diverted towards the inner wall, leaving a substantial CFL near the outer wall (Fig. 6d–f). One would expect the RBCs to migrate towards the channel centreline under hydrodynamic lift when travelling along CB11 (even with minimal shear-induced diffusion of cells in the dilute regime), therefore gradually recovering the inner-wall CFL and reducing the CFL asymmetry. However, there are two reasons why the CFL symmetry is not yet restored on arriving at BifT1. First, the length of CB11 is just 10 times its hydraulic diameter. Second,

as  $Q_2/Q_1$  increases, the flow velocity and the associated shear rate decreases in CB11. If the shear rate that RBCs experience becomes exceedingly low, RBCs appear rigid and tumble (resembling rigid-body rotation), rather than tank-tread. Tumbling RBCs experience a lower lift force than tank-treading RBCs.<sup>64</sup>

To examine whether the above conjecture is the case, we compare the motion of RBCs at a moderate  $Q_2/Q_1 = 3$  (Fig. 7b and c) with a high  $Q_2/Q_1 = 19$  (Fig. 7d and e). A notable difference in the RBC entry position in CB11 between  $Q_2/Q_1 = 3$  (near channel centre) and  $Q_2/Q_1 = 19$  (near inner wall) can be observed, which directs the cells to flow towards a different downstream branch or different sides of the same downstream branch. For  $Q_2/Q_1 = 3$ , the cells perform a “frisbee-like” spinning motion with nearly fixed orientation relative to the streamlines, accompanied by a slight increase in cell-wall distance (see the inset between Fig. 7b and c). This spinning behaviour has been previously captured in RBC experiments using simple shear flow, and is a transient motion regime towards tank-treading under increasing shear.<sup>65</sup> For  $Q_2/Q_1 = 19$ , the cells in CB11 are tumbling all the way along streamlines, and no sign of cross-streamline

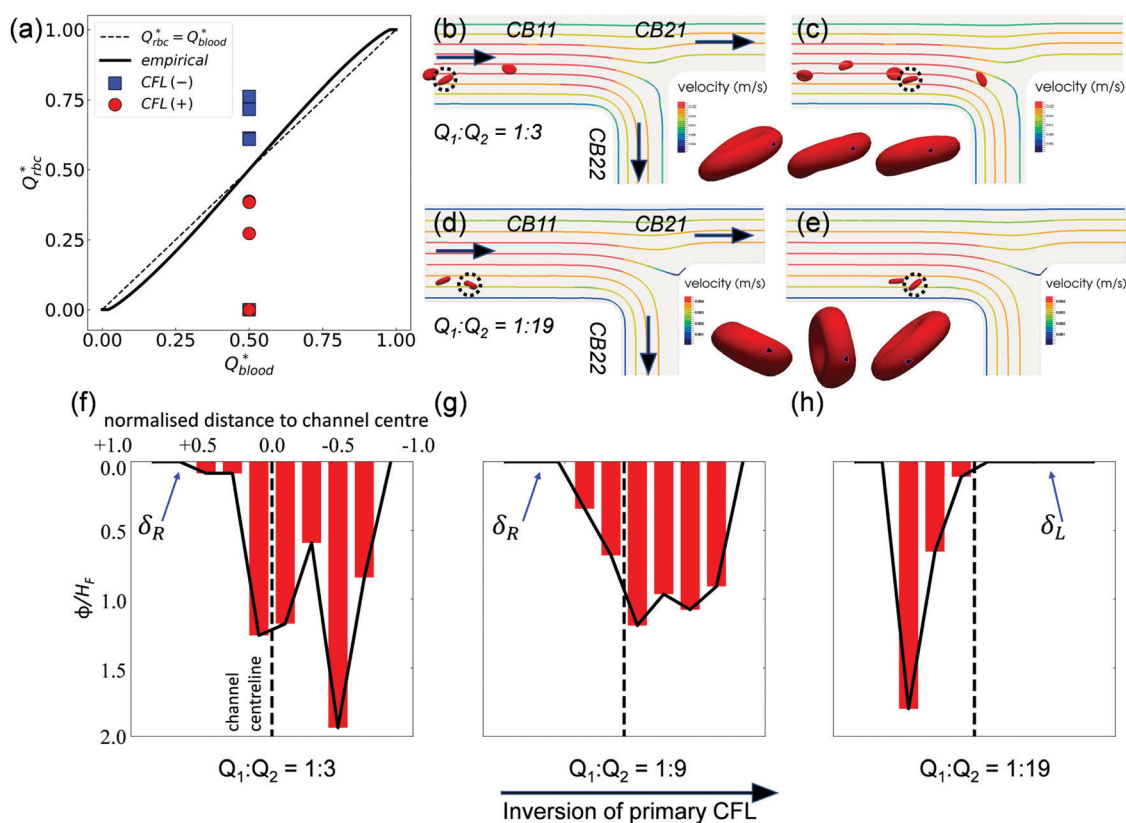


**Fig. 7** (Simulation) (a) Comparison of the simulated distribution of RBC fluxes at BifT1 against the empirical model,<sup>17</sup> following the same convention as Fig. 4e. (b and c) RBC motion in CB11 for  $Q_2/Q_1 = 3$ . The highlighted cell (dotted circle) spins forward with nearly fixed orientation. (d and e) RBC motion in CB11 for  $Q_2/Q_1 = 19$ . The highlighted cell tumbles in a rigid-body fashion. The black spot (triangle-shaped) on the highlighted cell in (b and c) and in (d and e) tracks a fixed mass element on the RBC membrane. An additional time instant between (b and c) and between (d and e) is also shown in the time sequence to better reflect the motion regime of the cell. (f–h) Haematocrit profiles (time-averaged distribution of local RBC concentration  $\phi$ , normalised by the feeding haematocrit  $H_F$ ) in channel CB22 under  $Q_2/Q_1 = 3, 9$ , and  $19$ , respectively. The CFL is defined as the region where  $\phi/H_F = 0$ . The primary CFL labelled as  $\delta_R$  or  $\delta_L$  indicates the side possessing a larger CFL within a channel, where “R” (right) or “L” (left) is relative to the flow direction (see black arrows in (b and d)).



migration can be observed (see the inset between Fig. 7d and e). The above two differences – the role of initial position and the dynamic mode of RBCs – both depend on the ratio of outflow rates  $Q_2/Q_1$  and co-determine the RBC trajectories at the T-bifurcation.

Notably, an inversion of the primary CFL location in CB22 occurs as the flow ratio is increased from  $Q_2/Q_1 = 9$  to 19 (Fig. 7g and h). This inversion primarily arises from the difference in the initial position of RBCs upon entering CB11, because the nominal shear rates in CB11 for  $Q_2/Q_1 = 9$  to  $Q_2/Q_1 = 19$  are designed in a way that the capillary number  $Ca$  is nearly the same under both flow conditions (see Table S1 in the ESI†).

### 3.4 Haematocrit reduction/enrichment in network

The partitioning of RBCs at successive bifurcations gives rise to a heterogeneity in the cell concentration throughout the network, especially with the presence of excessive outflow ratios (see Fig. 4b–d). To systematically quantify the RBC fluxes within the network and determine the preferential paths of RBCs, we calculate the discharge haematocrits  $H_D$  in all branches using a cell-counting procedure as stated in Section 2.3, and compare  $H_D$  to the discharge haematocrit  $H_{D,inflow}$  in the feeding branch of the whole network, *i.e.* PB (Table 2, see raw data in Table S3, ESI†). It is important to note that  $H_D$  itself is not a conserved quantity at a bifurcation (*e.g.*  $H_D^{PB} \neq H_D^{CB11} + H_D^{CB12}$ ); instead, the RBC flux  $Q_{rbc}$  is (*e.g.*  $Q_{rbc}^{PB} = Q_{rbc}^{CB11} + Q_{rbc}^{CB12}$ ), provided that the system is in a quasi steady state.

**3.4.1 Dilute suspensions.** We begin with the dilute regime,  $H_F = 1\%$ , which is the case for all simulation data presented so far (Table 2). For  $Q_2/Q_1 = 1$ , when our simulated network matches the scenario studied by Pries *et al.* representing a symmetric and regular topology<sup>60</sup> (free of the pathway effect<sup>66</sup>), the same observation is found for the mean  $H_D$  in downstream generations of the network (averaged among all branches in a given generation), which keeps constant relative to  $H_{D,inflow}$  as postulated by mass conservation. However, as the outflow ratio increases from  $Q_2/Q_1 = 1$  to 39, we observe a gradual decrease of the mean  $H_D/H_{D,inflow}$  from 1.00 to 0.51, which applies to both the 1st and 2nd generations. This reduction of  $H_D$  in higher generations of a vascular network should be distinguished from the Fåhræus effect, which leads to axial migration of cells

within single channels and causes the dynamic reduction in tube haematocrit ( $H_T$ ).<sup>67,68</sup> Instead, it should be attributed to the generalised “network Fåhræus effect”, which arises from geometrical heterogeneity within the network (*e.g.* difference in vessel length, diameter).<sup>60,69</sup>

Earlier on in Section 3.2, we have covered that when RBCs encounter the BifY with uneven fractional flows downstream (*i.e.*  $Q_2/Q_1 \neq 1$  at the outlets), asymmetric phase-separation between CB11 and CB12 occurs (Fig. 6). As  $Q_2/Q_1$  increases from 3 to 39, the degree of haematocrit reduction in CB11 is found to surge, with  $H_D/H_{D,inflow}$  dropping from 0.79 to zero (Table 2). The haematocrit enrichment in CB12 is not enhanced, but slightly decreased ( $H_D/H_{D,inflow}$  dropping from 1.07 to 1.02). Among the branches in the second generation of the network, CB21 is the most diluted branch under all investigated flow ratios, whereas CB23 is always most concentrated. The discharge haematocrits in CB23 and CB24 vary non-monotonically with  $Q_2/Q_1$ .

We further evaluate the  $H_D$  data at all three bifurcations separately using the PSM.<sup>17</sup> This empirical model matches well with simulation data at the BifY (Fig. 8a), but it breaks down at BifT1 and BifT2 (Fig. 8b and c). These findings are in line with our results in Sections 3.1–3.3 which demonstrated that the partitioning of RBCs at the BifY adheres to the Zweifach–Fung effect, whereas that at both BifTs is substantially biased due to the persisting CFL asymmetry in the respective feeding branches (CB11 and CB12). Notably, the range of haematocrit partition in branches downstream of BifT1 under even flow split is much wider than for BifT2, as a result of the stronger CFL asymmetry in CB11 compared to CB12 (see Fig. 5).

**3.4.2 Semidilute suspensions.** In addition to the  $H_F = 1\%$  simulations covering  $Q_2/Q_1$  between 1 and 40, the case of  $Q_2/Q_1 = 9$  is also repeated for  $H_F = 2\%$  and  $H_F = 10\%$  in order to investigate the effect of feeding haematocrit. The overall trend of reduction/enrichment in RBC perfusion remains unchanged, with haematocrit enrichment found for CB12 and CB23 and haematocrit reduction for other branches (see Table 2). Also, CB21 and CB23 are still the most diluted and most concentrated branches, respectively. The degree of haematocrit reduction (defined as relative decrease in  $H_D$  of a branch against  $H_{D,inflow}$ ) for CB21 for the three cases ( $H_F = 1\%, 2\%, 10\%$ ) decreases from  $-67\%$  to  $-55\%$ . Similarly, the degree of haematocrit enrichment (defined analogously) also drops, varying from 24% to 12%. Nevertheless, the mean  $H_D/H_{D,inflow}$  within each generation is nearly the same for the three cases, ranging between 0.82–0.85.

The cross-sectional haematocrit profiles (characterised through local RBC concentration  $\phi$ ) further reveal rich behaviour of the RBC distribution cascading down the network. Taking  $Q_2/Q_1 = 9$ ,  $H_F = 10\%$  as example (Fig. 9), the profile of  $\phi$  remains symmetric about the channel centreline in the main channel until approaching BifY, where an asymmetry starts to develop (see  $x = 350 \mu\text{m}$  in Fig. 9b). The asymmetry embedded in the  $\phi$  profile significantly grows in CB11 (see ROI5), resulting from distinct CFLs formed near opposite walls (Fig. 9c). Due to the

**Table 2** (Simulation) Ratio of  $H_D/H_{D,inflow}$  measured in the network (see definition in Section 2.3). The feeding haematocrit is  $H_F = 1\%$ , unless otherwise stated. If any child branch has  $H_D/H_{D,inflow} > 1$ , it experiences haematocrit enrichment; if  $H_D/H_{D,inflow} < 1$ , the branch experiences haematocrit reduction. The generation mean of  $H_D$  is obtained by averaging  $H_D$  in all child branches within the same generation

| $Q_2/Q_1$          | Individual branches |      |      |      |      |      |      | Generation mean |      |      |
|--------------------|---------------------|------|------|------|------|------|------|-----------------|------|------|
|                    | PB                  | CB11 | CB12 | CB21 | CB22 | CB23 | CB24 | 0th             | 1st  | 2nd  |
| 1                  | 1                   | 1.02 | 0.99 | 0.78 | 1.24 | 1.21 | 0.78 | 1               | 1.00 | 1.00 |
| 3                  | 1                   | 0.79 | 1.07 | 0.61 | 0.97 | 1.13 | 0.98 | 1               | 0.93 | 0.93 |
| 9                  | 1                   | 0.61 | 1.05 | 0.33 | 0.88 | 1.24 | 0.86 | 1               | 0.83 | 0.83 |
| 19                 | 1                   | 0.28 | 1.03 | 0.00 | 0.43 | 1.19 | 0.88 | 1               | 0.66 | 0.62 |
| 39                 | 1                   | 0.00 | 1.02 | 0.00 | 0.00 | 1.10 | 0.94 | 1               | 0.51 | 0.51 |
| 9 ( $H_F = 2\%$ )  | 1                   | 0.59 | 1.04 | 0.33 | 0.88 | 1.22 | 0.87 | 1               | 0.82 | 0.83 |
| 9 ( $H_F = 10\%$ ) | 1                   | 0.67 | 1.03 | 0.45 | 0.88 | 1.12 | 0.96 | 1               | 0.85 | 0.85 |



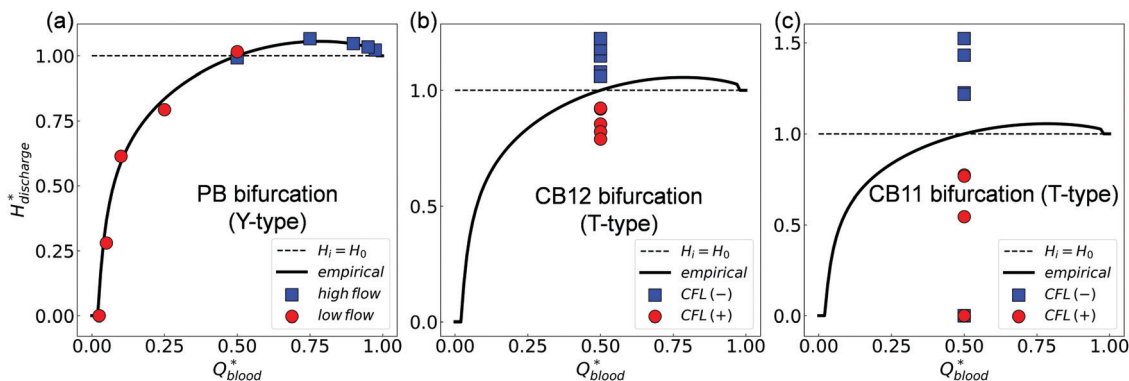


**Fig. 8** (Simulation) Comparison of simulated discharge haematocrits in each pair of child branches against the empirical PSM<sup>17</sup> for  $H_F = 1\%$  (raw data in Table S3, ESI†). (a) Y-type BifY (data corresponding to Fig. 4e). (b) T-type BifT2. (c) T-type BifT1 (data corresponding to Fig. 7a). In (a–c),  $H_{\text{discharge}}^*$  and  $Q_{\text{blood}}^*$  represent the fractional discharge haematocrit and fractional blood flow in a given child branch relative to its parent branch within a bifurcation. In (a), the circles and squares represent the relatively lower-flow and higher-flow child branches, respectively. In (b) and (c), the circles and squares represent the CFL-favoured and CFL-unfavoured child branches (determined by the relative magnitude of CFL they inherit from the upstream feeding branch), respectively. The solid lines in (a–c) are the empirical predictions.

low-shear environment and negligible hydrodynamic lift of RBCs in CB11, the CFL asymmetry persists throughout the interbifurcation segment until BifT1 is met and consequently leads to asymmetric RBC partitioning despite an even flow split ( $H_D = 4.48\%$  in CB21 *versus*  $H_D = 8.84\%$  in CB22, Fig. 9d and e). The  $\phi$  profile and accompanying CFL in CB21 (see ROI6) are even more asymmetric (Fig. 9d). Contrary to CB11, CB12 (see ROI8) appears less disturbed and presents a pseudo-symmetric  $\phi$  profile with the lateral CFLs slightly favouring the outer wall (Fig. 9f). The partitioning of RBCs into CB24 (see ROI9) and CB23 (see ROI10) downstream of CB12 is still uneven, with  $H_D = 9.60\%$  for CB24 and  $H_D = 11.28\%$  for CB23. For both CB24 and CB23, the asymmetry in the  $\phi$  profile is amplified compared with their immediate parent CB12 (Fig. 9g–i).

## 4 Discussion

### 4.1 Simulated RBC morphology and dynamics

The simulated RBC morphology in our arteriole-level network (see Fig. S5 in the ESI†) agrees with recent observations of human RBCs under microcirculatory flow conditions with physiological viscosity contrast ( $\lambda \geq 5$ ) between the RBC cytosol and the suspending medium.<sup>61,62</sup> However, complex shapes such as the RBC polylobe are reproduced in the present simulations without viscosity contrast ( $\lambda = 1$ ), whereas recently attempted RBC simulations in microchannels with  $\lambda = 5$  failed to capture the polylobe structure.<sup>63</sup> This is counterintuitive because a high viscosity contrast (*e.g.*  $\lambda > 3.2$ ) was asserted as crucial for the formation of multi-lobed structures on the

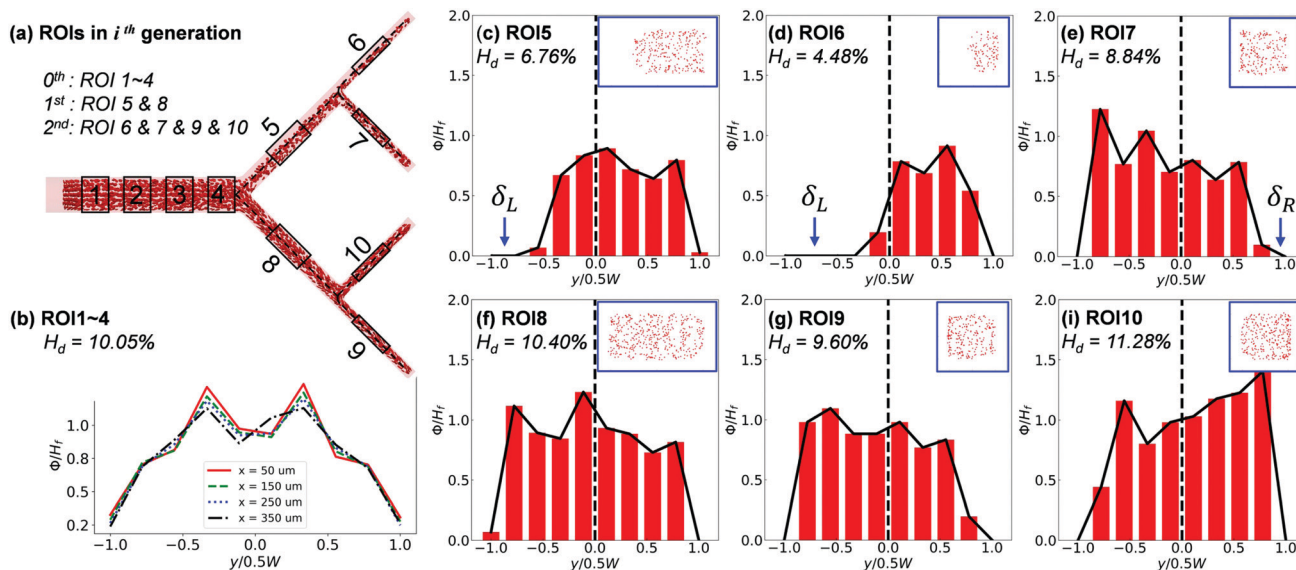


**Fig. 9** (Simulation) RBC distribution at  $Q_2/Q_1 = 9$  and  $H_F = 10\%$ . (a) Schematic of regions of interest (ROIs) selected for analysis. (b) Evolution of the haematocrit profile along the PB. Haematocrit profiles for branches located in (c–e) the upper half (low-flow portion) and (f–i) the lower half of the network (high-flow portion).  $\delta_R$  or  $\delta_L$  indicates the side of primary CFL. Insets in (c–i) show cross-sectional RBC distributions.



RBC membrane.<sup>62</sup> It is worth noting that previous simulations which reproduced the polylobe shape were either for simple shear flow<sup>61,62,70</sup> or planar Poiseuille flow<sup>71</sup> without the confinement of lateral walls.

A potential reason behind this disagreement is the confinement level  $\chi = \bar{D}_{\text{rbc}}/D_{\text{h}}$ , ratio of the RBC effective diameter ( $\bar{D}_{\text{rbc}} = 6.5 \mu\text{m}$ , diameter of a sphere with the same volume) to the channel hydraulic diameter. Whereas the confinement considered by the square-channel simulations in ref. 63 was between  $\chi = 0.4$ – $0.75$  (same confinement levels as their microfluidic experiments), the equivalent  $\chi$  in our current simulations is much lower, ranging between  $0.14$ – $0.22$ . Another source of the mismatch may be the membrane viscosity neglected by our simulations. Last but not least, a possible explanation for the polylobed RBCs observed in the present study could be the existence of transient secondary flows in the vicinity of a bifurcation, which is clearly absent in the configuration of simple or planar shear flows. Answering these questions with further observation from carefully designed experiments will advance our understanding of the mechanisms for dynamic RBC shapes in arteriole-level networks.

Apart from their evolving shapes, the motion regimes for RBCs observed in the simulated network is also rich, even for nearly unstressed cells with a biconcave shape. In addition to the commonly reported tumbling (in low shear) and tank-treading (in moderate/high shear) regimes, the intriguing “frisbee-like” spinning (a transient state between the rolling motion and tank-treading motion of RBCs under increasing shear as reported in ref. 65) is also reproduced by our simulations.

## 4.2 CFL development between arteriole-level bifurcations

Owing to its primary influence on the flow resistance as well as platelet/particle transport in microcirculatory blood flow, CFL has been extensively researched through *in vivo*, *in vitro* and *in silico* studies.<sup>72–74</sup> However, until recently most studies were focused on the variation of CFLs subject to different blood flow conditions in a single straight vessel/channel, and these discrete findings on CFL development may not be applicable to the microcirculation environment where bifurcations/junctions of diverse geometries are frequently met.<sup>22</sup> Our cell-scale simulation at successive arteriole-level bifurcations matching a microfluidic design of artificial vascular network provides a possibility of cross-validating numerical/experimental results with regard to CFL breakdown/recovery in complex geometries under finely-controlled flow conditions. This approach can be readily applied to query the spatio-temporal dynamics of heterogeneous RBC flow in more intricate microfluidic vascular networks presented earlier<sup>20,75</sup> and ultimately contribute to the formulation of reduced-order models for tractable blood flow simulation at larger scales, *e.g.* in tissue-level or organ-level vasculature.

Our simulated CFLs qualitatively agree with the experimental results, featuring symmetric CFL at opposite walls in the network feeding branch (see Fig. S6 in the ESI†) and increasingly asymmetric CFL in branches of downstream generations, especially under high network outflow ratios (see Fig. 3 for experimental observation and Fig. 5 for simulation data).

The origin of the CFL asymmetry observed here is rooted in the underdeveloped RBC flow between consecutive bifurcations, as their distance falls short for the perturbed haematocrit profile (*i.e.* transverse organisation of RBCs) to be sufficiently restored so that the symmetry of CFL can be re-established.

Whilst Pries *et al.* originally postulated a recovery length of  $10D$  (vessel diameter  $D \in [10,30] \mu\text{m}$ , *in vivo* measurements for rat mesenteric arterioles), Katanov *et al.*<sup>76</sup> revealed *via* 3D simulations that a length up to  $25D$  is needed for the CFL to fully develop in cylindrical microchannels ( $D \in [15,80] \mu\text{m}$ , haematocrit  $Ht \in [15\%,45\%]$ ). Also through simulations, Shaqfeh and co-workers<sup>71,77</sup> demonstrated moderately larger recovery lengths (beyond  $36D_{\text{h}}$ ) for the CFL to saturate in rectangular channels with comparable dimension and haematocrit levels (channel hydraulic diameter  $D_{\text{h}} \in [20,30] \mu\text{m}$ ,  $Ht \in [10\%,20\%]$ ). Under the circumstances of locally reduced flow or diluted RBC concentration in individual branches, the CFL recovery process may be further prolonged due to weakened hydrodynamic lift or lack of shear-induced diffusion. In our previous study of dilute RBC suspensions in low-inertia channel flow ( $D_{\text{h}} \approx 46 \mu\text{m}$ ,  $Ht \in [1\%, 5\%]$ ), a stationary CFL was not established even after  $46D_{\text{h}}$ .<sup>49</sup> The length required for the haematocrit profile to achieve equilibrium is in general more demanding, which can go beyond  $78D_{\text{h}}$  ( $D_{\text{h}} \approx 29 \mu\text{m}$ ) according to ref. 78.

## 4.3 Partitioning of RBCs at microvascular bifurcations

There are two main approaches for studies in the context of RBC partitioning at bifurcations. The first examines the relative motion of individual RBCs (or their biomimetic counterpart, vesicles or capsules) against the background flow in different bifurcation geometries (*e.g.* ref. 29, 30, 31, 32, 35, 36 and 79), typically aimed at microfluidic design optimisation for cell sorting or enrichment. The second approach focuses on quantifying the split of RBC fluxes or discharge haematocrits within a flowing RBC suspension at bifurcations (*e.g.* ref. 12, 13, 15, 21, 23 and 24), aimed at elucidating the fundamental process of phase separation occurring *in vivo* which may inspire not only enhanced blood-on-a-chip devices, but also novel strategies for treating microcirculatory disorders arising from abnormal blood flow.

Our cellular blood simulations involving successive bifurcations at the arteriole scale, in parallel with corroborating microfluidic experiments, provide exhaustive data for in-depth examination of the RBC partitioning behaviour through cross-validation between experimental and computational data. In particular, we investigate whether or not the classic phase separation of blood as stipulated by the Zweifach–Fung effect<sup>2</sup> and the empirical model<sup>8</sup> is observed, and how these observations are related to the individual motion of RBCs and the symmetry/asymmetry of CFLs preceding a bifurcation. We also validate a straightforward means of manipulating the RBC partitioning within a bifurcating network, *i.e.* by varying the flow ratios between network outlets, which consistently leads to certain branches developing excessive haematocrit reduction or enrichment at feeding haematocrits  $H_{\text{F}} = 1\%$ – $10\%$ .



#### 4.4 Implications and limitations

In summary, our computational model of cellular blood flow with highly resolved RBCs flowing in an artificial microvascular network satisfactorily reproduces the phenomenon of biased RBC partitioning observed in the corroborating microfluidic experiments. The simulations elucidate in detail the microscopic behaviour of RBCs at arteriole-level bifurcations (channel hydraulic diameter  $D_h = 30\text{--}50\ \mu\text{m}$ ) subject to different outflow ratios at terminal branches of the network. Furthermore, our findings suggest the prominent effect of CFL asymmetry on the phase separation process. Such CFL asymmetry arises from upstream disturbances and can persist for more than 10 times the hydraulic channel diameter, which plays a key role in the partitioning of RBCs in downstream branches.

Some important implications are: (I) Artificial microvascular networks consisting of rectangular microchannels designed following the biomimetic rule proposed by Zografos *et al.*<sup>46</sup> can capture the phase-separation process of RBC suspensions in realistic microvascular networks with quantitative accuracy (see Fig. 4e, evaluation performed against the established empirical model based on *in vivo* data from rat arteriolar bifurcations<sup>8</sup>), provided that equivalent dimensional descriptions are used, *e.g.* hydraulic channel diameter *versus* vessel diameter. (II) In low-inertia flows ( $Re < 1$ ) with arteriole-level confinement (relatively small  $D_{\text{rbc}}/D_h$ ), RBCs in dilute/semidilute suspensions follow the fluid streamlines in the vicinity of a bifurcation and behave like point particles, with no evident migration of RBC populations crossing the stagnation streamline (see Fig. S4d–f, ESI†). Therefore, the obstruction effect proposed by<sup>45</sup> or the low-flow attraction effect proposed by<sup>32</sup> is irrelevant, and the partitioning of RBCs obeys the classic Zweifach–Fung effect provided that the symmetry of haematocrit profile or CFL is preserved. Under such conditions, reduced models without involving RBCs may be sufficient to capture the phase-separation process. (III) Under high outflow ratios, RBCs near the stagnation streamline (separation surface or separatrix in 3D, which divides the fluid layers entering different branches) tend to be drawn towards the lower-flow branch first and linger for a while. They are then pulled away and eventually flow into the higher-flow branch (see Fig. 6d–f). This observation is in line with the finding of a previous numerical study in 2D, where similar behaviour was found for an elastic capsule.<sup>31</sup> An earlier microfluidic study of bifurcating channels at 180 degrees also presented similar pattern of RBC fluxes at a high ratio of fractional flows.<sup>48</sup> (IV) Significant asymmetry in both the CFL and haematocrit profile prevails in a vascular network as suggested by<sup>22,44</sup> earlier, owing to disrupted cross-sectional distribution of RBCs in downstream branches by the disturbance of upstream bifurcations (see Fig. 9). As a consequence, the partitioning of RBCs at successive bifurcations can be substantially biased and would give rise to excessive haematocrit reduction in downstream child branches, even under equal flow splits (see Fig. 8). (V) The lateral migration of RBCs, which arises from the hydrodynamic lift and contributes to the recovery of disrupted CFL, is largely suppressed in branches of low flow due to the

absence of tank-treading motion. This leads to negligible recovery of CFL symmetry between certain consecutive bifurcations.

There are several limitations for the present study. (1) While horse RBCs were used in experiments, the numerical model simulates human RBCs. This may have caused a certain degree of quantitative discrepancy between the simulation and experiments. However, the influence on results of the suspension behaviour should be limited to quantitative instead of qualitative differences (see evidence from our previous paper<sup>49</sup>). (2) Quantitative agreement of the CFL thickness as well as the critical outflow ratio for complete RBC depletion in low-flow fraction of the network between experiments and simulations remains challenging due to our numerical treatment of the flow entry region (required for tractable computational cost), where geometric contraction in the width direction is deliberately removed to enable the generation of an artificial CFL immediately after the inlet (see Section 2.2 for the reason behind this particular treatment). This numerical treatment is justified against our previous findings of CFL development of dilute RBC suspensions in low-inertia channel flow<sup>49</sup> (see Section S5 of the ESI†). (3) So far, only dilute/semidilute RBC suspensions ( $H_F = 1\%, 2\%, 10\%$ ) are simulated, primarily aimed at a mechanistic understanding of RBC partitioning behaviour in bifurcating microchannels. The performance of the biomimetic microfluidic network in terms of separating RBCs and plasma is subject to scrutiny if the haematocrit is to be further increased to a level when cell–cell interactions become dominant. As previously reported by ref. 13, the degree of phase-separation is expected to decrease with increasing haematocrit, especially for symmetric bifurcations. Our preliminary experiments with higher RBC concentration ( $H_F = 10\%, 20\%$ ) suggest less pronounced phase-separation even under extreme flow conditions (see Fig. S3 in the ESI†). The reduction/enrichment effect through controlling outflow ratios reported in the present study remains to be further inspected before applications are possible, *e.g.* handling dense RBC suspensions for separation, sorting or purification purposes.

## 5 Concluding remarks

This work studies the partitioning of RBCs in an artificial vascular network designed following a biomimetic rule that generalises Murray's law for microfluidic manifolds. The microscopic behaviour of RBCs flowing within are reported in detail, including their morphological deformation, motion regime, and temporal paths. We find the RBC partitioning at the primary bifurcation, where the symmetry of cross-sectional cell distribution in the feeding branch are preserved, quantitatively agreeing with the established phase-separation model<sup>8,17</sup> as an empirical approximation of the classic Zweifach–Fung effect. Contrarily at secondary bifurcations, a biased partitioning that substantially deviates from the empirical model is observed under moderate or high network outflow ratios, leading to excessive haematocrit reduction/enrichment in downstream child branches. The biased phase separation is attributed to the complex spatio-temporal dynamics of RBC flow within a



successively bifurcating network, featured by the post-bifurcation breakdown of CFL symmetry due to upstream disturbances on the cell distribution and the lack of symmetry recovery due to negligible hydrodynamic lift of cells tumbling in low-shear environments.

Whilst the Zweifach–Fung effect has been widely tested and validated to predict the partitioning of RBCs at individual bifurcations, our current results draw attention to exceptions in a network of bifurcations for which CFL asymmetries prevail in the system when the haematocrits are considerably lower than the physiological level and the flow rates in certain fraction of the network are small. Caution is therefore needed when applying the empirical phase-separation model<sup>8,17</sup> to describe blood flow in a hierarchical network, especially under non-physiological flow conditions as in the case of many microfluidic experiments. The qualitative and quantitative agreement between our simulations and experiments in an arteriole-level artificial network is important to validate the 3D computational model for studying the haemodynamics of cellular blood flow in diverse microfluidic devices or reconstructed microvascular networks. Our findings of the RBC partitioning within the bifurcating geometry may also find application in manipulating blood samples for biomedical purposes.

## Author contributions

QZ organised the research, performed the simulations, analysed the data and wrote the article. JF designed and conducted the experiments, processed the experimental data and analysed the results. MOB discussed the results and revised the manuscript. MSNO and TK conceived the research idea, supervised the study and edited the manuscript.

## Conflicts of interest

The authors declare that they have no competing financial interests.

## Acknowledgements

The authors would like to acknowledge the contribution of the *HemeLB* development team. QZ thanks the University of Edinburgh for the award of a Principal's Career Development Scholarship and an Edinburgh Global Research Scholarship. TK's and MOB's contributions have been sponsored through two Chancellor's Fellowships at the University of Edinburgh and funded by EPSRC (grant EP/T008806/1). TK is also funded by the European Commission (grant agreement No 803553). MOB is supported by grants from EPSRC (EP/R029598/1, EP/R021600/1), Fondation Leducq (17 CVD 03), and the European Unions Horizon 2020 research and innovation programme under grant agreement No. 801423. Supercomputing time on the ARCHER UK National Supercomputing Service (<http://www.archer.ac.uk>) was provided by the "UK Consortium on Mesoscale

Engineering Sciences (UKCOMES)" under the EPSRC Grant No. EP/R029598/1. Processing and disposal of the blood sample were performed following the Ethics Committee for Animal Experimentation at University of Strathclyde.

## References

- 1 A. S. Popel and P. C. Johnson, *Annu. Rev. Fluid Mech.*, 2005, **37**, 43–69.
- 2 K. Svanes and B. W. Zweifach, *Microvasc. Res.*, 1968, **1**, 210–220.
- 3 Y.-C. Fung, *Microvasc. Res.*, 1973, **5**, 34–48.
- 4 A. Krogh, *J. Physiol.*, 1921, **55**, 412–422.
- 5 G. W. Schmid-Schönbein, R. Skalak, S. Usami and S. Chien, *Microvasc. Res.*, 1980, **19**, 18–44.
- 6 G. Mchedlishvili and M. Varazashvili, *Biorheology*, 1982, **19**, 613–620.
- 7 B. Klitzman and P. C. Johnson, *Am. J. Physiol.*, 1982, **242**, H211–H219.
- 8 A. R. Pries, K. Ley, M. Claassen and P. Gaehtgens, *Microvasc. Res.*, 1989, **38**, 81–101.
- 9 B. M. Fenton, R. T. Carr and G. R. Cokelet, *Microvasc. Res.*, 1985, **29**, 103–126.
- 10 R. T. Carr and L. L. Wickham, *Microvasc. Res.*, 1991, **41**, 184–196.
- 11 S. Yang, A. Ündar and J. D. Zahn, *Lab Chip*, 2006, **6**, 871–880.
- 12 J. M. Sherwood, D. Holmes, E. Kaliviotis and S. Balabani, *PLoS One*, 2014, **9**, e100473.
- 13 S. Roman, A. Merlo, P. Duru, F. Risso and S. Lorthois, *Biomicrofluidics*, 2016, **10**, 034103.
- 14 Z. Shen, G. Coupier, B. Kaoui, B. Polack, J. Harting, C. Misbah and T. Podgorski, *Microvasc. Res.*, 2016, **105**, 40–46.
- 15 K. Yamamoto, H. Abe, C. Miyoshi, H. Ogura and T. Hyakutake, *J. Med. Biol. Eng.*, 2020, **40**, 53–61.
- 16 A. R. Pries, T. W. Secomb, P. Gaehtgens and J. F. Gross, *Circ. Res.*, 1990, **67**, 826–834.
- 17 A. R. Pries, B. Reglin and T. W. Secomb, *Am. J. Physiol.*, 2003, **284**, H2204–H2212.
- 18 A. R. Pries and T. W. Secomb, *Am. J. Physiol.*, 2005, **289**, H2657–H2664.
- 19 P. M. Rasmussen, T. W. Secomb and A. R. Pries, *Microcirculation*, 2018, **25**, e12445.
- 20 O. Forouzan, X. Yang, J. M. Sosa, J. M. Burns and S. S. Shevkoplyas, *Microvasc. Res.*, 2012, **84**, 123–132.
- 21 A. Mantegazza, F. Clavica and D. Obrist, *Biomicrofluidics*, 2020, **14**, 014101.
- 22 P. Balogh and P. Bagchi, *J. Fluid Mech.*, 2019, **864**, 768–806.
- 23 M. O. Bernabeu, J. Köry, J. A. Grogan, B. Markelc, A. Beardo, M. d'Avezac, R. Enjalbert, J. Kaeppler, N. Daly, J. Hetherington, T. Krüger, P. K. Maini, J. M. Pitt-Francis, R. J. Muschel, T. Alarcón and H. M. Byrne, *Proc. Natl. Acad. Sci. U. S. A.*, 2020, **117**, 27811–27819.
- 24 T. Hyakutake and S. Nagai, *Microvasc. Res.*, 2015, **97**, 115–123.



- 25 G. Enden and A. S. Popel, *J. Biomech. Eng.*, 1994, **116**, 79–88.
- 26 J. O. Barber, J. M. Restrepo and T. W. Secomb, *Cardiovascular Engineering and Technology*, 2011, **2**, 349–360.
- 27 H. Ye, H. Huang and X.-Y. Lu, *Comput. Fluids*, 2015, **114**, 110–120.
- 28 T. Wang, U. Rongin and Z. Xing, *Sci. Rep.*, 2016, **6**, 20262.
- 29 J. O. Barber, J. P. Alberding, J. M. Restrepo and T. W. Secomb, *Ann. Biomed. Eng.*, 2008, **36**, 1690–1698.
- 30 W. Xiong and J. Zhang, *Biomech. Model. Mechanobiol.*, 2012, **11**, 575–583.
- 31 H. C. Woolfenden and M. G. Blyth, *J. Fluid Mech.*, 2011, **669**, 3–31.
- 32 V. Doyeux, T. Podgorski, S. Peponas, M. Ismail and G. Couplier, *J. Fluid Mech.*, 2011, **674**, 359–388.
- 33 K. Lykov, X. Li, H. Lei, I. V. Pivkin and G. E. Karniadakis, *PLoS Comput. Biol.*, 2015, **11**, e1004410.
- 34 T. Ye, L. Peng and Y. Li, *J. Appl. Phys.*, 2018, **123**, 064701.
- 35 Z. Wang, Y. Sui, A.-V. Salsac, D. Barthès-Biesel and W. Wang, *J. Fluid Mech.*, 2016, **806**, 603–626.
- 36 Z. Wang, Y. Sui, A.-V. Salsac, D. Barthès-Biesel and W. Wang, *J. Fluid Mech.*, 2018, **849**, 136–162.
- 37 T. Ye, L. Peng and G. Li, *Biomech. Model. Mechanobiol.*, 2019, **18**, 1821–1835.
- 38 Z. L. Liu, J. R. Clausen, J. L. Wagner, K. S. Butler, D. S. Bolintineanu, J. B. Lechman, R. R. Rao and C. K. Aidun, *Phys. Rev. E*, 2020, **102**, 013310.
- 39 X. Yin, T. Thomas and J. Zhang, *Microvasc. Res.*, 2013, **89**, 47–56.
- 40 S. S. Ye, M. Ju and S. Kim, *Microvasc. Res.*, 2016, **106**, 14–23.
- 41 C. Bächer, A. Kihm, L. Schrack, L. Kaestner, M. W. Laschke, C. Wagner and S. Gekle, *Biophys. J.*, 2018, **115**, 411–425.
- 42 P. K. Ong, S. Jain and S. Kim, *Microvasc. Res.*, 2012, **83**, 118–125.
- 43 Y. C. Ng, B. Namgung, S. L. Tien, H. L. Leo and S. Kim, *Am. J. Physiol.*, 2016, **311**, H487–H497.
- 44 P. Balogh and P. Bagchi, *Phys. Fluids*, 2018, **30**, 051902.
- 45 R. W. Barber and D. R. Emerson, *Microfluid. Nanofluid.*, 2008, **4**, 179–191.
- 46 K. Zografos, R. W. Barber, D. R. Emerson and M. S. N. Oliveira, *Microfluid. Nanofluid.*, 2015, **19**, 737–749.
- 47 J. Fidalgo, K. Zografos, L. Casanellas, A. Lindner and M. S. N. Oliveira, *Biomicrofluidics*, 2017, **11**, 064106.
- 48 J. Fidalgo, D. Pinho, R. Lima and M. S. N. Oliveira, *Vip-IMAGE 2017*, Cham, 2018, pp. 945–953.
- 49 Q. Zhou, J. Fidalgo, L. Calvi, M. O. Bernabeu, P. R. Hoskins, M. S. N. Oliveira and T. Krüger, *Biophys. J.*, 2020, **118**, 2561–2573.
- 50 T. Krüger, *Computer Simulation Study of Collective Phenomena in Dense Suspensions of Red Blood Cells under Shear*, Vieweg + Teubner Verlag, 2012.
- 51 M. D. Mazzeo and P. V. Coveney, *Comput. Phys. Commun.*, 2008, **178**, 894–914.
- 52 M. O. Bernabeu, M. L. Jones, J. H. Nielsen, T. Krüger, R. W. Nash, D. Groen, S. Schmieschek, J. Hetherington, H. Gerhardt, C. A. Franco and P. V. Coveney, *J. R. Soc., Interface*, 2014, **11**, 20140543.
- 53 Y. H. Qian, D. D’Humières and P. Lallemand, *EPL*, 1992, **17**, 479.
- 54 P. L. Bhatnagar, E. P. Gross and M. Krook, *Phys. Rev.*, 1954, **94**, 511–525.
- 55 Z. Guo, C. Zheng and B. Shi, *Phys. Rev. E: Stat., Nonlinear, Soft Matter Phys.*, 2002, **65**, 046308.
- 56 M. Bouzidi, M. Firdaouss and P. Lallemand, *Phys. Fluids*, 2001, **13**, 3452–3459.
- 57 A. J. C. Ladd, *J. Fluid Mech.*, 1994, **271**, 285–309.
- 58 C. S. Peskin, *Acta Numerica*, 2002, **11**, 479–517.
- 59 T. Krüger, F. Varnik and D. Raabe, *Computers & Mathematics with Applications*, 2011, **61**, 3485–3505.
- 60 A. R. Pries, T. W. Secomb and P. Gaetgens, *Am. J. Physiol.*, 1996, **270**, H545–H553.
- 61 L. Lanotte, J. Mauer, S. Mendez, D. A. Fedosov, J.-M. Fromental, V. Claveria, F. Nicoud, G. Gompper and M. Abkarian, *Proc. Natl. Acad. Sci. U. S. A.*, 2016, 201608074.
- 62 J. Mauer, S. Mendez, L. Lanotte, F. Nicoud, M. Abkarian, G. Gompper and D. A. Fedosov, *Phys. Rev. Lett.*, 2018, **121**, 118103.
- 63 F. Reichel, J. Mauer, A. A. Nawaz, G. Gompper, J. Guck and D. A. Fedosov, *Biophys. J.*, 2019, **117**, 14–24.
- 64 A. Nait-Ouhra, A. Guckenberger, A. Farutin, H. Ez-Zahraouy, A. Benyoussef, S. Gekle and C. Misbah, *Phys. Rev. Fluids*, 2018, **3**, 123601.
- 65 J. Dupire, M. Socol and A. Viallat, *Proc. Natl. Acad. Sci. U. S. A.*, 2012, **109**, 20808–20813.
- 66 A. R. Pries, T. W. Secomb and P. Gaetgens, *Am. J. Physiol.*, 1995, **269**, H1713–H1722.
- 67 K. H. Albrecht, P. Gaetgens, A. R. Pries and M. Heuser, *Microvasc. Res.*, 1979, **18**, 33–47.
- 68 R. Skalak and S. Chien, *Biorheology*, 1981, **18**, 307–330.
- 69 A. R. Pries, K. Ley and P. Gaetgens, *Am. J. Physiol.*, 1986, **251**, H1324–H1332.
- 70 N. Takeishi, M. E. Rosti, Y. Imai, S. Wada and L. Brandt, *J. Fluid Mech.*, 2019, **872**, 818–848.
- 71 A. Saadat, C. J. Guido and E. S. G. Shaqfeh, bioRxiv:10.1101/572933, 2019.
- 72 S. Kim, P. K. Ong, O. Yalcin, M. Intaglietta and P. C. Johnson, *Biorheology*, 2009, **46**, 181–189.
- 73 D. A. Fedosov, B. Caswell, A. S. Popel and G. E. Karniadakis, *Microcirculation*, 2010, **17**, 615–628.
- 74 S. Tripathi, Y. V. B. V. Kumar, A. Prabhakar, S. S. Joshi and A. Agrawal, *J. Micromech. Microeng.*, 2015, **25**, 083001.
- 75 N. Z. Piety, W. H. Reinhart, J. Stutz and S. S. Shevkoplyas, *Transfusion*, 2017, **57**, 2257–2266.
- 76 D. Katanov, G. Gompper and D. A. Fedosov, *Microvasc. Res.*, 2015, **99**, 57–66.
- 77 Q. M. Qi and E. S. G. Shaqfeh, *Phys. Rev. Fluids*, 2018, **3**, 034302.
- 78 H. Zhao, E. S. G. Shaqfeh and V. Narsimhan, *Phys. Fluids*, 2012, **24**, 011902.
- 79 G. Li, T. Ye, S. Wang, X. Li and R. UI Haq, *Phys. Fluids*, 2020, **32**, 031903.

